J. Cent. South Univ. (2015) 22: 2482−2492
DOI: 10.1007/s11771-015-2776-3

Springer

CFD simulation of effect of anode configuration on gas–liquid flow and alumina transport process in an aluminum reduction cell

ZHAN Shui-qing(詹水清)[1], LI Mao(李茂)[1], ZHOU Jie-min(周孑民)[1],
YANG Jian-hong(杨建红)[2], ZHOU Yi-wen(周益文)[2]

1. School of Energy Science and Engineering, Central South University, Changsha 410083, China;
2. Zhengzhou Research Institute, Aluminum Corporation of China Ltd., Zhengzhou 450041, China

Abstract: Numerical simulations of gas–liquid two-phase flow and alumina transport process in an aluminum reduction cell were conducted to investigate the effects of anode configurations on the bath flow, gas volume fraction and alumina content distributions. An Euler–Euler two-fluid model was employed coupled with a species transport equation for alumina content. Three different anode configurations such as anode without a slot, anode with a longitudinal slot and anode with a transversal slot were studied in the simulation. The simulation results clearly show that the slots can reduce the bath velocity and promote the releasing of the anode gas, but can not contribute to the uniformity of the alumina content. Comparisons of the effects between the longitudinal and transversal slots indicate that the longitudinal slot is better in terms of gas–liquid flow but is disadvantageous for alumina mixing and transport process due to a decrease of anode gas under the anode bottom surface. It is demonstrated from the simulations that the mixing and transfer characteristics of alumina are controlled to great extent by the anode gas forces while the electromagnetic forces (EMFs) play the second role.

Key words: aluminum reduction cell; anode configuration; gas–liquid flow; alumina transport process; simulation; alumina content distribution

1 Introduction

When alumina is fed into an aluminum reduction cell, its dissolution, diffusion and transport process starts in the molten cryolite bath. Also, the anode gas (mainly carbon dioxide) is mainly generated under the anode bottom surface and moves up through the bath under the influence of buoyancy and recirculation flows. The anode gas induces bath flow in the cell, which plays an important positive role in homogenization of the alumina concentration. Due to the large surface area of the anode, the anode gas gradually gathers under the anode bottom surface, therefore, a certain thickness of gas layer can be formed. Conversely, this gas layer can increase voltage drop, which in turn results in high energy consumption during the electrolytic process [1].

So far, a large number of studies were performed to predict gas-induced bath flow behaviors in an aluminum reduction cell using computational fluid dynamics (CFD) methods. Different CFD models have been employed to obtain reasonably and detailed gas–liquid flow hydrodynamics based on Euler–Euler, Euler–Lagrangian or volume of fluid (VOF) approach [2–8]. These CFD simulations were mainly focused on obtaining the bulk flow behaviors, such as the liquid velocity field, the liquid turbulence and gas volume fraction distribution.

Recently, more attention has been paid to investigating the alumina distribution in the cells. For example, FENG et al [9−10] studied the effects of various design parameters on the gas-induced bath flow and alumina mixing in a typical full-scale industrial cell without considering electromagnetic forces (EMFs). THOMAS [11] investigated the dissolution process of alumina and the optimization of alumina feeder configuration using simulation method with custom subroutines. ZHANG [12] used a transient multi-component and multi-phase flow model to simulate the alumina transport process and the optimization allocation of alumina feeders. KAENEL et al [13] developed a mathematical model to study the alumina convection and diffusion process coupled with the cell magneto-hydrodynamic (MHD) model in the presence of small bubbles due to the slotted anodes.

Foundation item: Project(2010AA065201) supported by the High Technology Research and Development Program of China; Project(2013zzts038) supported by the Fundamental Research Funds for the Central Universities of China; Project(ZB2011CBBCe1) supported by the Major Program for Aluminum Corporation of China Limited, China
Received date: 2014−06−24; **Accepted date:** 2014−09−17
Corresponding author: LI Mao, Associate Professor, PhD; Tel: +86−13055169363; E-mail: limao89@163.com

However, there are many important issues remaining unresolved in these CFD simulations, especially the detailed and accurate alumina dissolution and transport process. ZHAN et al [14] studied the gas–bath two-phase flow that occurs during the alumina transport process in the melts of an aluminum reduction cell by using an Euler–Euler two-fluid model coupled with a transport equation of alumina concentration. Besides, more reasonable alumina dissolution and consumption models were involved [15]. Almost all the studies reached the same conclusion: the bath flow played an important role in the alumina transport process.

It is well known that slots in the anodes are effective in reducing the voltage drop due to anode gas [16]. This is because the slots allow a better discharge of the gas from the anode bottom surface. But, so far, there have been few studies on CFD simulations of the gas and bath flows as well as the slotted anodes, especially for the alumina transport process. Depending on the specific extrusion direction, the slotted anodes can be made longitudinal or transversal. SEVERO et al [17] presented a CFD model to investigate the effects of different slotted anodes on the gas driven bath flow. YANG and COOKSEY [18] numerically and experimentally studied the effects of the slot width and height on the bath flow under various cell operation conditions. The effects of the longitudinal, transversal and vertical slot cutting at anodes on gas elimination process with CFD simulation were discussed by YANG et al [19]. It can be seen from the above discussion that, despite the aforementioned CFD simulations and experimental studies on slot designs, systematic and detailed investigations of the effects of the slotted anodes on the fluid dynamics, especially on the distribution characteristics of anode gas and alumina concentration inside the cells are still greatly desired by industry.

In present work, the fully gas–liquid two-phase flow and alumina transport process in a 300 kA aluminum reduction cell were simulated and analyzed using an Euler–Euler approach. The primary objective of the work was to investigate the effects of different anode configurations on the bath flow, gas volume fraction and alumina content distributions with detailed discussion employing the CFD simulations.

2 Mathematical modeling

In the present work, the mathematical model is formulated based on the Euler–Euler two-fluid model, in which both continuous and dispersed phases are considered as interpenetrating continuous media. The Reynolds averaged mass and momentum balance equations in turbulent flow regime, without considering the interfacial mass transport and reaction, can be written as

$$\frac{\partial}{\partial t}(\rho_k \alpha_k) + \nabla \cdot (\rho_k \alpha_k \boldsymbol{u}_k) = 0 \tag{1}$$

$$\frac{\partial(\alpha_k \rho_k \boldsymbol{u}_k)}{\partial t} + \nabla \cdot (\alpha_k \rho_k \boldsymbol{u}_k \boldsymbol{u}_k) = \alpha_k \nabla \cdot \boldsymbol{P} + \nabla \cdot (\alpha_k \mu_{\text{eff}} \nabla \boldsymbol{u}_k) + \nabla \cdot (\alpha_k \mu_{\text{eff}} \nabla \boldsymbol{u}_k)^{\text{T}} + \boldsymbol{S}_k + \boldsymbol{F}_k \tag{2}$$

where the indice k denotes the continuous phase ("L" for liquid) or the dispersed phase ("G" for gas). α_k, ρ_k and $\boldsymbol{u}_k$ are the volume fraction, density and time-average velocity of phase k, respectively. μ_{eff} is effective viscosity of phase k and $\boldsymbol{P}$ is the pressure, which is shared by both phases. $\boldsymbol{S}_k$ is the momentum sources due to external body forces on the phase k, which mainly include EMFs and buoyancy. $\boldsymbol{F}_k$ is the interfacial forces acting on phase due to the presence of other phases, which mainly include drag force (F_{D}) and non-drag force (F_{ND}). In addition, the sum of volume fractions is an unity:

$$\sum_{k=1}^{2} \alpha_k = 1 \tag{3}$$

The formulation used in the present work assumes that the effective viscosity of the liquid phase consists of three contributions: the molecular viscosity μ_{L}, the turbulence viscosity $\mu_{\text{t,L}}$, and an additional term due to bubble induced turbulence $\mu_{\text{BI,L}}$, i.e.

$$\mu_{\text{eff,L}} = \mu_{\text{L}} + \mu_{\text{t,L}} + \mu_{\text{BI,L}} \tag{4}$$

There are several models available for accounting the turbulence induced by the movement of the bubbles. In this work, the model proposed by SATO et al [20] is used:

$$\mu_{\text{BI,L}} = C_{\mu\text{B}} \rho_{\text{L}} \alpha_{\text{G}} d_{\text{B}} |\boldsymbol{u}_{\text{G}} - \boldsymbol{u}_{\text{L}}| \tag{5}$$

where the standard model constant $C_{\mu\text{B}}$ is equal to 0.6.

In the present model, the simulation only considers the drag force between the liquid and gas phases but ignores the non-drag force. The modified expression of drag force considering both the volume fraction of the gas and liquid phases can be written as

$$F_{\text{D}} = 0.75 \alpha_{\text{G}} (1 - \alpha_{\text{G}}) \rho_{\text{L}} (C_{\text{D}} / d_{\text{B}}) |\boldsymbol{u}_{\text{G}} - \boldsymbol{u}_{\text{L}}| (\boldsymbol{u}_{\text{G}} - \boldsymbol{u}_{\text{L}}) \tag{6}$$

where the drag coefficient C_{D} can be described by an empirical drag law proposed by Schiller−Naumann model [21] and is given by

$$C_{\text{D}} = \begin{cases} \dfrac{24}{Re}\left(1 + 0.15 Re^{0.687}\right), & Re \le 1000 \\ 0.44, & Re > 1000 \end{cases} \tag{7}$$

$$Re = \frac{\rho_{\text{L}} |\boldsymbol{u}_{\text{G}} - \boldsymbol{u}_{\text{L}}| d_{\text{B}}}{\mu_{\text{L}}} \tag{8}$$

where d_{B} is the bubble diameter, Re is the relative Reynolds number, and μ_{L} is viscosity of liquid phase.

A modified two-phase k–ε turbulence model is used to solve the transport equations for the turbulent kinetic energy k and its dissipation rate ε by assuming the pseudo bath turbulence resulted from anodic gas. In this model, turbulent predictions for the bath phase are obtained using the standard k–ε model supplemented with extra terms that include the inter-phase turbulent momentum transfer. Predictions for turbulence quantities for the gas phase are obtained using the Tchen theory of dispersion of discrete bubbles by homogeneous turbulence [21]. The transport equations of k and ε are as follows:

$$\frac{\partial}{\partial t}\left(\alpha_{\mathrm{L}}\rho_{\mathrm{L}}k_{\mathrm{L}}\right)+\nabla\cdot\left(\alpha_{\mathrm{L}}\rho_{\mathrm{L}}k_{\mathrm{L}}\boldsymbol{u}_{\mathrm{L}}\right)=\nabla\cdot\left(\alpha_{\mathrm{L}}\frac{\mu_{\mathrm{t,L}}}{\delta_k}\nabla k_{\mathrm{L}}\right)+\alpha_{\mathrm{L}}G_{k,\mathrm{L}}-\alpha_{\mathrm{L}}\rho_{\mathrm{L}}\varepsilon_{\mathrm{L}}+\alpha_{\mathrm{L}}\rho_{\mathrm{L}}\Pi_{k,\mathrm{L}} \tag{9}$$

$$\frac{\partial}{\partial t}\left(\alpha_{\mathrm{L}}\rho_{\mathrm{L}}\varepsilon_{\mathrm{L}}\right)+\nabla\cdot\left(\alpha_{\mathrm{L}}\rho_{\mathrm{L}}\varepsilon_{\mathrm{L}}\boldsymbol{u}_{\mathrm{L}}\right)=\nabla\cdot\left(\alpha_{\mathrm{L}}\frac{\mu_{\mathrm{t,L}}}{\delta_\varepsilon}\nabla\varepsilon_{\mathrm{L}}\right)+\alpha_{\mathrm{L}}\frac{\varepsilon_{\mathrm{L}}}{k_{\mathrm{L}}}\left(C_{1\varepsilon}G_{k,\mathrm{L}}-C_{2\varepsilon}\rho_{\mathrm{L}}\varepsilon_{\mathrm{L}}\right)+\alpha_{\mathrm{L}}\rho_{\mathrm{L}}\Pi_{\varepsilon,\mathrm{L}} \tag{10}$$

$$\mu_{\mathrm{t,L}}=\rho_{\mathrm{L}}C_\mu\frac{k_{\mathrm{L}}^2}{\varepsilon_{\mathrm{L}}} \tag{11}$$

where the standard model constants are $C_{1\varepsilon}$=1.44, $C_{2\varepsilon}$=1.92, C_μ=0.09, δ_k=1.0 and δ_ε=1.3. The term $G_{k,\mathrm{L}}$ represents the generation of turbulent kinetic energy and is computed from

$$G_{k,\mathrm{L}}=\frac{1}{2}\mu_{\mathrm{t,L}}\left[\nabla\boldsymbol{u}_{\mathrm{L}}+\left(\nabla\boldsymbol{u}_{\mathrm{L}}\right)^{\mathrm{T}}\right]^2 \tag{12}$$

It should be noted that the bath phase in aluminum reduction cells is mainly comprised of two components, i.e., cryolite and alumina. The species transport equation of alumina (species i), described in terms of local mass fraction or mass concentration is modeled as

$$\frac{\partial}{\partial t}\left(\alpha_{\mathrm{L}}\rho_{\mathrm{L}}Y_{\mathrm{L},i}\right)+\nabla\cdot\left(\alpha_{\mathrm{L}}\rho_{\mathrm{L}}Y_{\mathrm{L},i}\boldsymbol{u}_{\mathrm{L}}\right)=\nabla\cdot\left[\alpha_{\mathrm{L}}\left(\rho_{\mathrm{L}}D_{\mathrm{L},i}+\frac{\mu_{\mathrm{t,L}}}{Sc_{\mathrm{t,L}}}\left(\nabla Y_{\mathrm{L},i}\right)\right)\right]+S_{\mathrm{L},i} \tag{13}$$

where $Y_{\mathrm{L},i}$ and $D_{\mathrm{L},i}$ are the mass fraction and effective diffusion coefficient of alumina, respectively. $S_{\mathrm{L},i}$ is the mass transfer source related to the source of alumina dissolution and consumption in the cells. $Sc_{\mathrm{t,L}}$ is the Schmidt number. The details of the alumina dissolution model verified by related experiment results and consumption model have been discussed in our previous work [14−15] and will not be covered in this work.

3 Simulation methods

The gas–liquid two-phase flow and alumina transport process in a 300 kA aluminum reduction cell was studied as an application case in this work. A rectangular box model, which has the dimensions close to real cells with alumina feeding positions and other structure parameters, is shown in Fig. 1. This cell is a rectangular steel shell with the volume of 14.46 m (long)×3.76 m (wide)×0.20 m (high). The anode-cathode distance (ACD) is set to be 0.05 m. The widths of the inter-anode channel, the side one, the end one and the center one are 0.04 m, 0.20 m, 0.25 m and 0.18 m, respectively. The cell consists of 20×2 anodes named A1−A20 and B1−B20, respectively. Three different anode configurations, i.e., anode without a slot, anode with a longitudinal slot and anode with a transversal slot, were chosen as model anodes in the simulation, as shown in Fig. 2. The width and height of both the longitudinal and transversal slots are 20 mm and 300 mm, respectively. There are four alumina feeding points, with each hopper being 1.8 kg of alumina, which were modeled in an arrangement called inter-anode feeders located at the intersection positions of central channel and inter-anode channel. Alumina was fed as a source term of species transport equation in a region of 160 mm×160 mm×20 mm, with the top surface of the region being at the bath. One normal feeding cycle length is set to be 144 s and the four feeders are conducted simultaneously. The 300 kA aluminum reduction cell is meshed in hexahedral cells by means of the Fluent preprocessor Gambit.

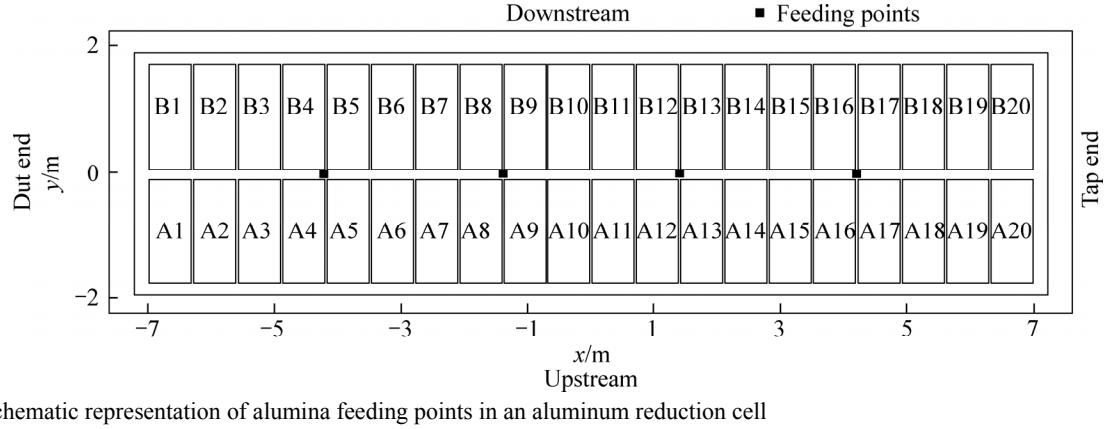

Fig. 1 Schematic representation of alumina feeding points in an aluminum reduction cell

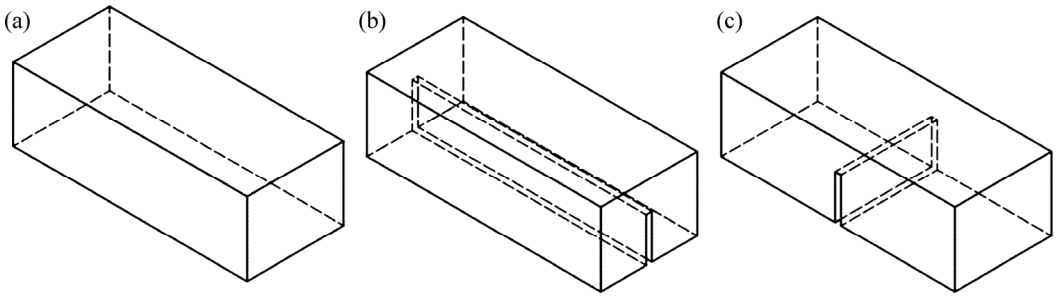

Fig. 2 Schematic representation of three different anode configurations used in CFD simulations: (a) Anode without a slot; (b) Anode with a longitudinal slot; (c) Anode with a transversal slot

In the simulations, the anode bottom surface was treated as a mass-flow-inlet boundary condition with inlet gas volume fraction of 0.5. The mass flow rates of anode gas generation of 3.08×10^{-2}, 2.98×10^{-2} and 3.04×10^{-2} kg/s for three different anode configurations respectively introduced above were obtained by a known Faraday's laws of electrolysis. The mass flow rate is determined by the anode gas generation rate at the unit anode bottom q which can be calculated as follows:

$$q=\frac{JRT}{4FP} \tag{14}$$

where J is the anodic current density, 0.7 A/cm^2; R is the universal gas constant, 8.314 J/(mol·K); T is the absolute temperature, 1223 K; F is known Faraday's constant, 96485 C/mol; P is atmosphere pressure, 101325 Pa.

The top surface of the bath was considered as a degassing boundary, which was seen by the continuous phase as a free-slip wall and as an outlet by the dispersed gas phase. No-slip boundary conditions were used for both phases at the wall of the cells, where the standard wall function was used for the turbulence equations.

In this work, the commercial CFD software, Fluent, was used to simulate the gas–liquid flow and alumina transport process. The phase-coupled SIMPLE algorithm was used to couple pressure and momentum equations. The second order upwind discretization scheme was chosen for all the equations. The under-relaxation factors for pressure, momentum, volume fraction and alumina transport equations used in the model were 0.2, 0.2, 0.2 and 0.5, respectively. Under the same conditions, a validation simulation based on full-scale three anode cells has been conducted and the results obtained were compared with experimental data [22] under similar conditions using particle image velocimetry (PIV), as reported in previous work [5]. Good agreement was found between the bath flow over the four vertical planes predicted by CFD model and by PIV measurement.

Initially, only the flow equations with two phases were solved to obtain a quasi-steady flow field considering the average EMFs computed with ANSYS using the mesh-to-mesh solution interpolation, since the mesh used in ANSYS and Fluent is different. Then, the species transport equation of alumina was activated and solved coupled with other governing equations. Considering the time scale of transfer process of alumina in the cell, the time step was fixed at 0.05 s through the feeding cycles. Initially, the alumina content was set to be 2.5% (mass fraction) throughout the entire computational domain at the start of the simulation. The mesh-to-mesh solution interpolation for EMFs, the species transport equation source accounting for alumina feeding and alumina consumption were all defined through user-defined functions (UDFs). All the physical parameters used in the CFD simulation are listed in Table 1.

Table 1 Physical parameters used in CFD simulation

Physical parameter	Value
ρ_L/(kg·m^{-3})	2130
ρ_G/(kg·m^{-3})	0.398
μ_L/(kg·m^{-1}·s^{-1})	2.51×10^{-3}
μ_G/(kg·m^{-1}·s^{-1})	5.05×10^{-5}
D/(m^2·s^{-1})	1.5×10^{-9}
M/(g·mol^{-1})	102
η/%	93
V/m^3	10.43

4 Results and discussion

4.1 Effect of anode configuration on gas volume fraction distribution

Gas volume fraction is one of the most important parameters, which is used to characterise the interfacial mass. Previous CFD studies have shown that the anode designs significantly affect the overall gas volume fraction and local gas volume fraction [6, 19]. Figure 3 shows the overall gas volume fraction distributions for three different anode configurations. As shown in Fig. 3, the anode gas mainly exists in the ACD, with only very small amounts in the other areas. Besides, the gas volume fraction in the inter-anode channel is higher than

that in the center channel. This is because the gas prefers to travel along the shortest path and more gas escapes from the inter-anode channel than from the center channel. Moreover, the slots in the anodes act as an additional inter-anode gap, so the anode gas can escape vertically from the slots. The existence of such slots causes the quick entrainment of the anode gas from the anode bottom. As a result, the volume fraction becomes lower in the center channel when using the slots, which can be observed obviously from Figs. 3(a) and (b).

The gas volume fraction distributions at a horizontal plane with a distance of 10 mm from the anode bottom surface in the ACD for different anode configurations are shown in Fig. 4. It can be seen from Fig. 4 that the anode without a slot produces the highest gas volume fraction while the anode with a longitudinal slot yields the lowest gas volume fraction and the gas volume fraction for the anode with a transversal slot lies somewhere in between them. The gas layer has a thin square shape, with higher gas volume fraction in central area, but lower in boundary area. This can be attributed to the fact that the use of a slot gives rise to an extremely strong escape of anode gas and the gas residence time gets short. Therefore, the gas volume fraction is lower for the anode with a slot than that for the anode without a slot. The effects of the longitudinal and transversal slots look similar to the inter-anode and center channel, respectively. So, such a phenomenon leads to a lower gas volume fraction for the anode with a longitudinal slot than that for the anode with a transversal slot, as shown in Figs. 4(b) and (c).

In order to further demonstrate more details of the gas layer, Fig. 5 shows the gas volume fraction distribution at a vertical plane in the inter-anode channel for the anode without a slot. As shown in Fig. 5, a careful enlarged observation of the gas layer from Fig. 4(a) reveals that the farther away from the anode bottom is, the lower the gas volume fraction is. It is also indicated that when the z-section is less than 0.23 m, the gas volume fraction is generally close to 0, which means that the height of the gas layer is almost 20 mm for the anode without a slot. Table 2 gives the comparison of the calculated gas average volume fraction at different z-sections in ACD for different anode configurations. Three different heights of z-section are defined, i.e., z-5 mm, z-10 mm and z-15 mm, respectively, which stand for certain distance (5, 10, 15 mm, respectively) from the anode bottom surface. It can be seen from Table 2, for each z-section, the gas average volume fraction is in the order of the anode without a slot > the anode with a transversal slot > the anode with a longitudinal slot. From this, we can infer that the height of gas layer is in the order of the anode without a slot > the anode with a transversal slot > the anode with a longitudinal slot. The existence of the gas layer has different effects on the interaction between the gas and bath phase flow at different heights of z-section, which has a vital impact on the bath flow and alumina concentration distribution in the cell.

4.2 Effect of anode configuration on bath velocity distribution

Figure 6 shows the bath velocity distributions at a horizontal plane in the middle of the ACD for different

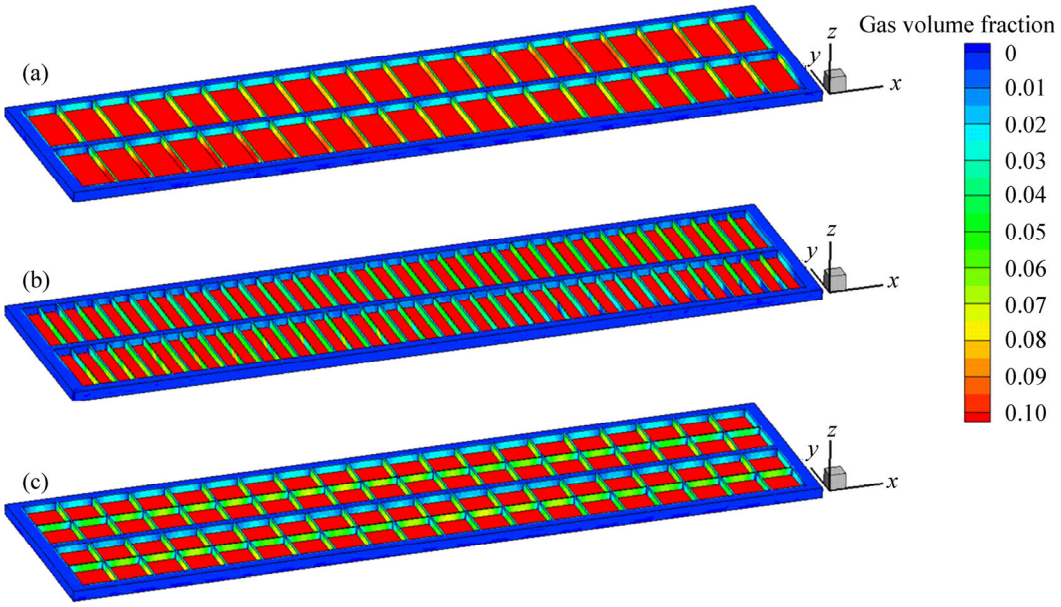

Fig. 3 Overall gas volume fraction distributions for three different anode configurations (red represents gas volume fraction larger than 0.1): (a) Without slot; (b) Longitudinal slot; (c) Transversal slot

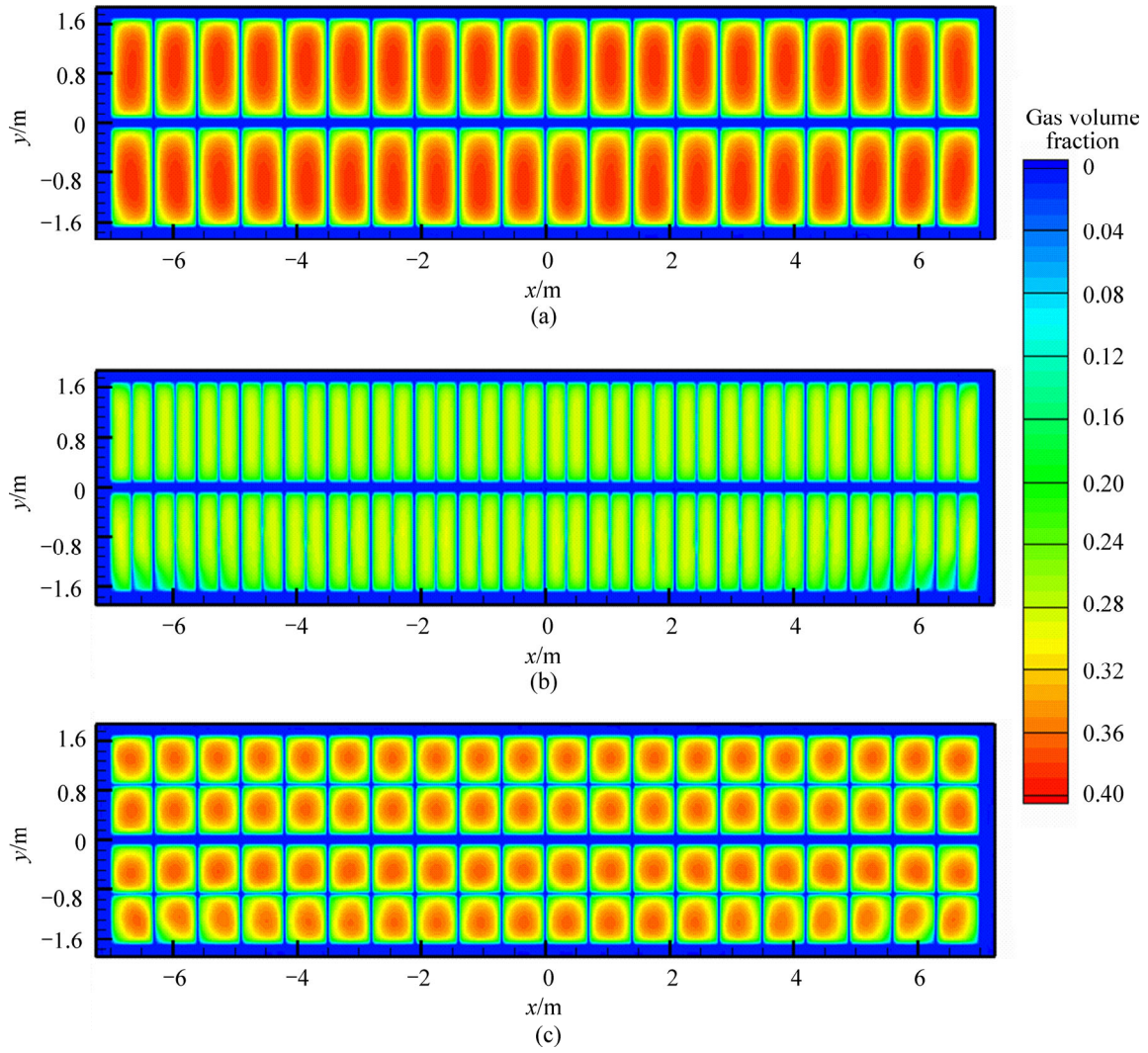

Fig. 4 Gas volume fraction distributions at a horizontal plane (10 mm from anode bottom) in ACD for three different anode configurations: (a) Without slot; (b) Longitudinal slot; (c) Transversal slot

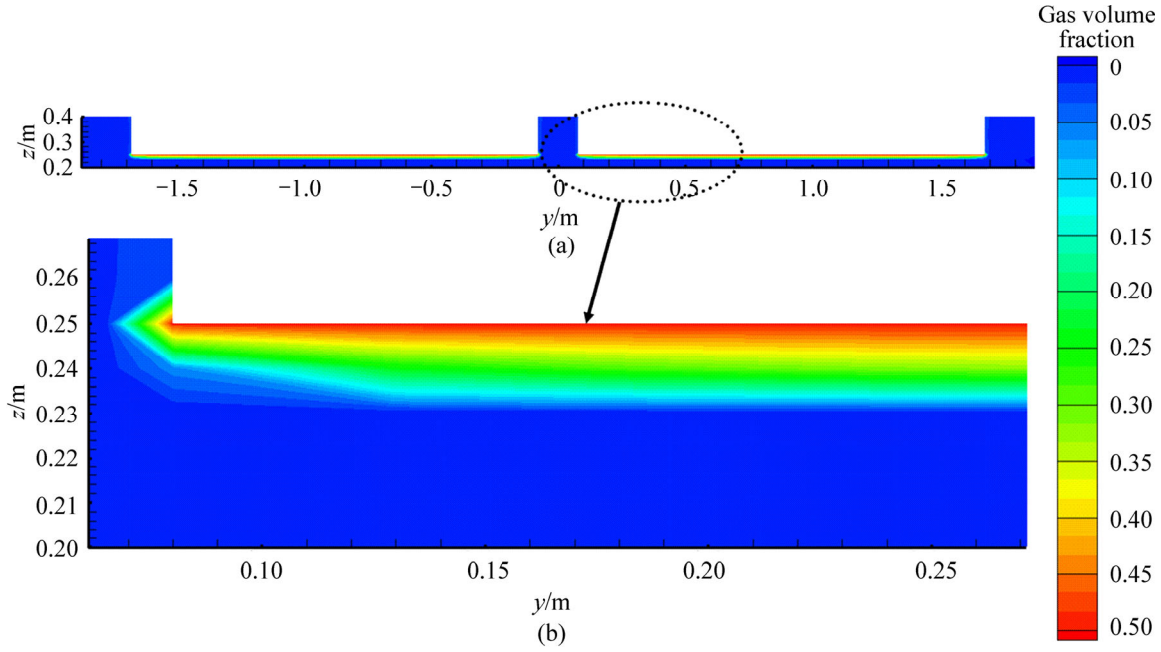

Fig. 5 Gas volume fraction distributions at a vertical plane in middle of anodes for anode without a slot

Table 2 Comparison of calculated gas average volume fraction for three different anode configurations

Anode	Gas average volume fraction/%		
	z-5 mm	*z*-10 mm	*z*-15 mm
Without slot	40.07	32.19	24.31
Longitudinal slot	39.02	28.47	17.42
Transversal slot	39.54	30.63	21.42

anode configurations. Streamlines have been plotted to identify the overall flow distribution that is more intuitive than expected. From Fig. 6, it can be seen that the bath velocity distributions for the anode with a longitudinal or a transversal slot is similar to that for the anode without a slot. As a whole, in the three cases, the bath flow has two large roughly circulations with approximately symmetrical eddies and a series of small eddies around each anode. It is also indicated that the bath velocity magnitude is larger near both the side and end channels than that underneath all the anodes. The main difference of the bath velocity distribution for the anode with and without a slot is the characteristic of the small eddies and its great influence on the two large eddies. Besides, smaller local recirculation zones around each anode due to the inducement of the additional rising anode gas flow can be found for the anode with a slot, as shown in Figs. 6(b) and (c). There is a little increase in the bath velocity in the slots, especially for the anode with a transversal slot. The bath average velocity for the anode without a slot, with a longitudinal slot and a transversal slot are 7.31, 6.13 and 6.76 cm/s, respectively. The effect of the transversal or longitudinal slot is to reduce the average bath velocity under the anode bottom for flow stability. In general, the two large eddies due to the EMFs and lots of small eddies due to anode gas forces may form the key component of the bath velocity distribution. As a result, the characteristic of the bath flow field will significantly influence the dissolution and transport process of alumina, which may affect alumina concentration distribution.

4.3 Effect of anode configuration on alumina content distribution

In our previous work [14], it was described that both the anode gas forces and EMFs have significant impact on the bath flow field. In addition, the anode gas forces have certain effect on the uniformity of alumina content only in some local positions but the EMFs have a

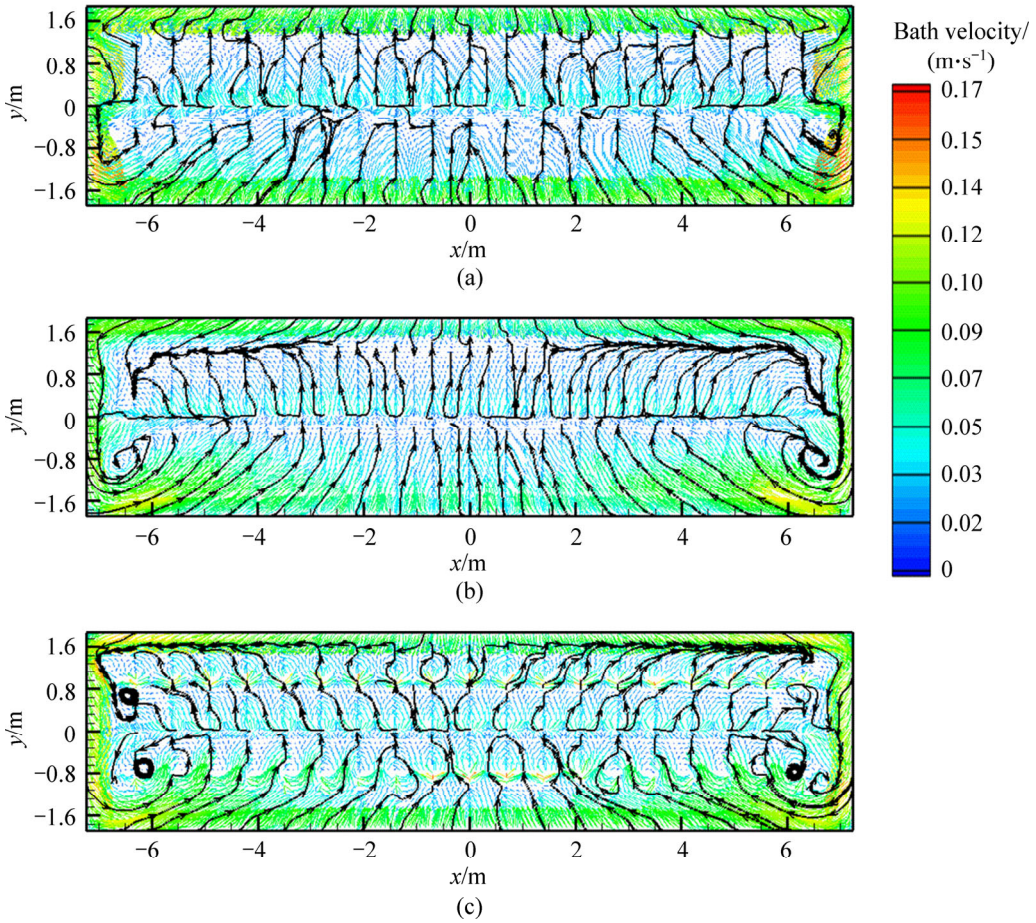

Fig. 6 Bath velocity distribution at a horizontal plane in middle of ACD for three different anode configurations: (a) Without slot; (b) Longitudinal slot; (c) Transversal slot

wider range of influence and a more effective transport process for the alumina in the full cell. More importantly, the alumina content distribution can eventually reach a periodic state because of alumina mass conservation, and this final periodic state is independent of the initial alumina condition but dependent very much on the bath flow field. The periodic state for the anode without a slot under the combined effects of both the anode gas forces and EMFs is reached after about 1152 s (about eight feeding cycles). In order to save computer time and to simplify simulations in this work, only ten normal feeding cycles are simulated for the three different anode configurations and only the simulated results of the tenth cycle (t=1296−1440 s) are studied, which seems very reasonable from the view point of simplifying the practicable engineering problem.

In order to further demonstrate the relationship between bath flow field and alumina content distribution, the transient alumina content variations for three velocity fields have been investigated. In the three simulated cases considered here, it appears that the arrangements of the feeding points are the same, so significant changes to the bath flow field due to the different anode configurations are unable to overcome the effects of the feeding points. Only the transient alumina content distributions at a horizontal plane in the middle of the ACD during the tenth cycle for the anode without a slot are illustrated in Fig. 7. It can be seen that the high alumina content zones exist only near the feeding points after a short time of feeding (Fig. 7(b)). Then, the alumina dissolved near the left two feeding points goes along the direction of the left circulation path and the alumina dissolved near the right two feeding positions moves to the right circulation path. With the progress of alumina transport process, more and more alumina is dissolved and transported to the whole bath with two large eddies. From Figs. 7(b)–(e), it appears that the high alumina content zones shrink gradually and the uniformity of alumina content can be attained once again. The characteristics of alumina content distribution follow the flow characteristics of the bath, which is more obvious in later stages of this feeding cycle (Figs. 7(c)–(f)). The results suggest that the alumina content distribution is obviously affected by the bath flow field, because the convective mass transfer dominates. Comparisons between the alumina content distributions in Figs. 7(a) and (f) indicate that the alumina content distributions are almost the same at the start and end of one feeding cycle, indirectly demonstrating the periodic state reported previously. Thus, the transient alumina content distributions can help to better understand the flow regularities in the bath and the relationship between them.

In this work, the standard deviation of the alumina content is used as an index to evaluate the uniformity of alumina content. The alumina content distribution is more homogenized with low standard deviation. The standard deviation of the alumina content on a surface is computed using the mathematical expression:

$$\sigma=\sqrt{\frac{\sum_{i=1}^{n}(C-C_0)^2}{n}} \tag{15}$$

where C is the discrete cell value of the alumina content at each facet in the simulation, C_0 is the average value of C, and n is the total number of facets.

Figure 8 shows the standard deviations of alumina

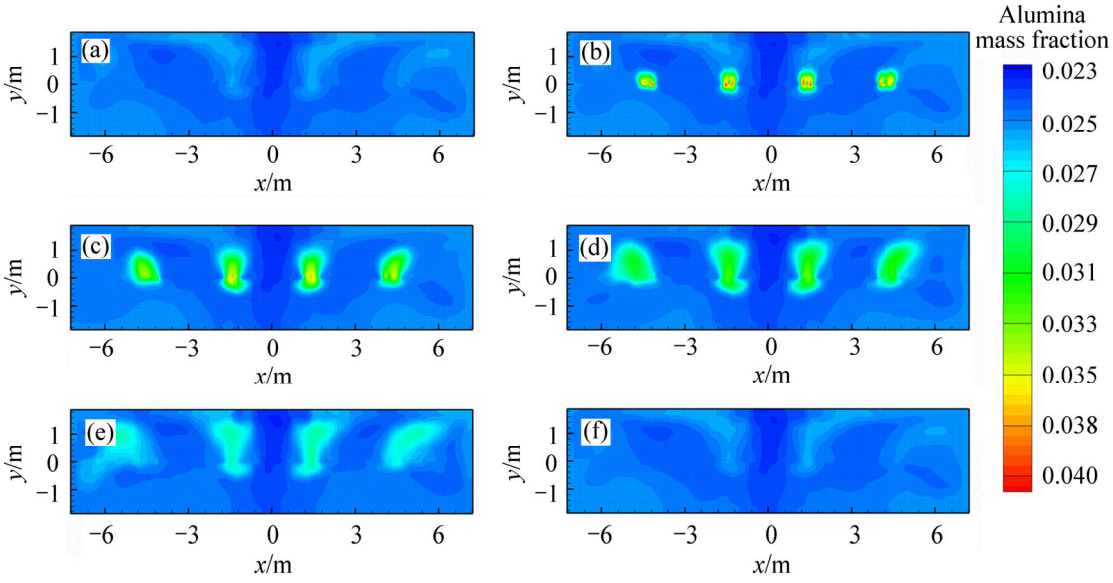

Fig. 7 Transient alumina content distributions at a horizontal plane in middle of ACD during tenth cycle for anode without a slot: (a) 1296 s; (b) 1304 s; (c) 1320 s; (d) 1340 s; (e) 1380 s; (f) 1440 s

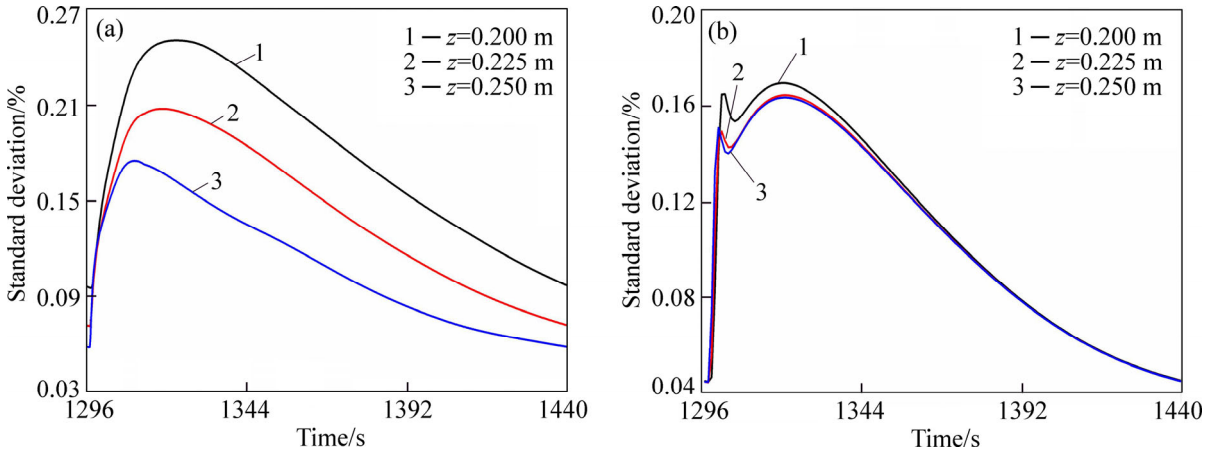

Fig. 8 Standard deviation of alumina content at different horizontal sections in ACD during the tenth cycle for anode without a slot: (a) Only under EMFs; (b) Under anode gas forces and EMFs

content at different horizontal sections in ACD during the tenth cycle for the anode without a slot. On the whole, the standard deviation at each horizontal section increases firstly and then decreases, mainly due to the different rates of alumina dissolution and consumption at different time periods, the diffusion of the content difference and the transport process followed by the bath flow. A detailed comparison between Figs. 8(a) and (b) explains the effect of anode gas forces and EMFs on the uniformity of alumina, respectively. When the bath flow field is influenced only by the EMFs, the standard deviation can vary gradiently. And the closer to the anode bottom, the smaller the standard deviation. But when the bath flow field is affected by both the anode gas forces and EMFs, the standard deviation at each horizontal section in Fig. 8(b) becomes smaller than that in Fig. 8(a). Besides, the gradient of the standard deviations between z=0.225 m and z=0.25 m becomes much smaller than that between z=0.2 m and z=0.225 m. Obviously, this is likely associated with the homogenization effect of anode gas in the flow, so that the alumina transport and mixing process can benefit from the gas-induced bath flow in the cells. This phenomenon is more apparent in the gas layer where the anode gas mainly remains. More details of the homogenization effect of the anode gas forces for the anode with a slot will be discussed further later.

Alumina content distributions at a horizontal plane in the middle of the ACD for different anode configurations at the tenth cycle are shown in Fig. 9. It can be seen from Fig. 9 that some low and high alumina contents appear almost at the same areas for the three cases. Some low alumina contents appear obviously almost under the anodes B10−B11 and A10−A11, and some high alumina contents appear obviously almost under the anodes B8−B9 and B12−B13, and in the end and side channels. Besides, a careful observation from Fig. 9 reveals that the area of low alumina content for the anode with a longitudinal slot (Fig. 9(b)) is slightly larger than that for the anode without a slot (Fig. 9(a)).

Figure 10 shows the comparison of the standard deviations of alumina content at different z-sections in the ACD during the tenth cycle for different anode configurations (both anode gas forces and EMFs). It can be seen from Fig. 10 that, for each horizontal section, the standard deviation of alumina content is in the order of the anode without a slot < the anode with a transversal slot < the anode with a longitudinal slot. This is likely associated with the induction of the slots so that the strong and quick escape of the additional anode gas can cause a significant decrease of the strength of induced circulation by gas under the anode bottom. Therefore, the homogenization effect of anode gas would be weakened, which is not good for the alumina transport and mixing process in the cells. A comparison of the standard deviation between cases for the anode with a transversal slot and a longitudinal slot reveals that the former can reach a better alumina content uniformity than the latter because a notable increase of gas volume fraction is achieved in the gas layer for the anode with a transversal slot, as shown in Fig. 4 and Table 2. But the anode with a transversal slot shows little effect on the uniformity compared with the anode without a slot. It seems that the alumina content distribution is controlled to great extent by the anode gas generated under the anode bottom surface while the EMFs also play the second role. It can be postulated that there exists an optimum bath flow field and corresponding gas dispersion type for the alumina mixing and transport in the aluminum reductions cell, which can be obtained by optimising the anode configurations.

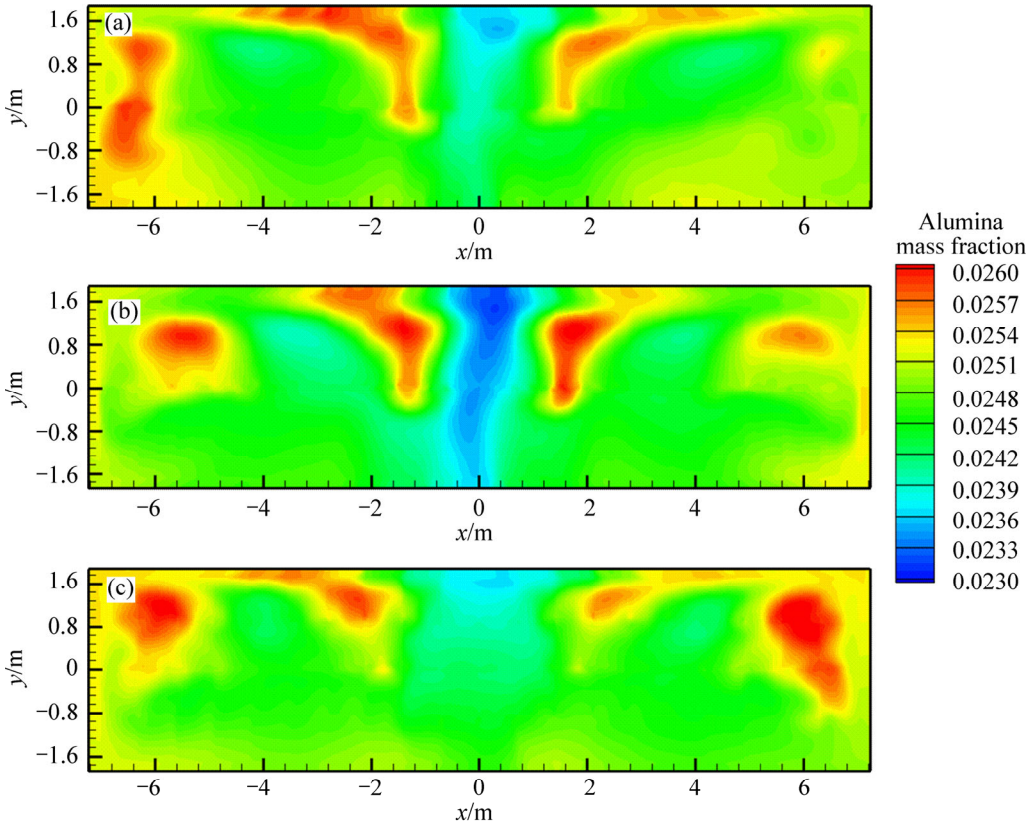

Fig. 9 Alumina content distributions at a horizontal plane in middle of ACD for three different anode configurations: (a) Without slot; (b) Longitudinal slot; (c) Transversal slot

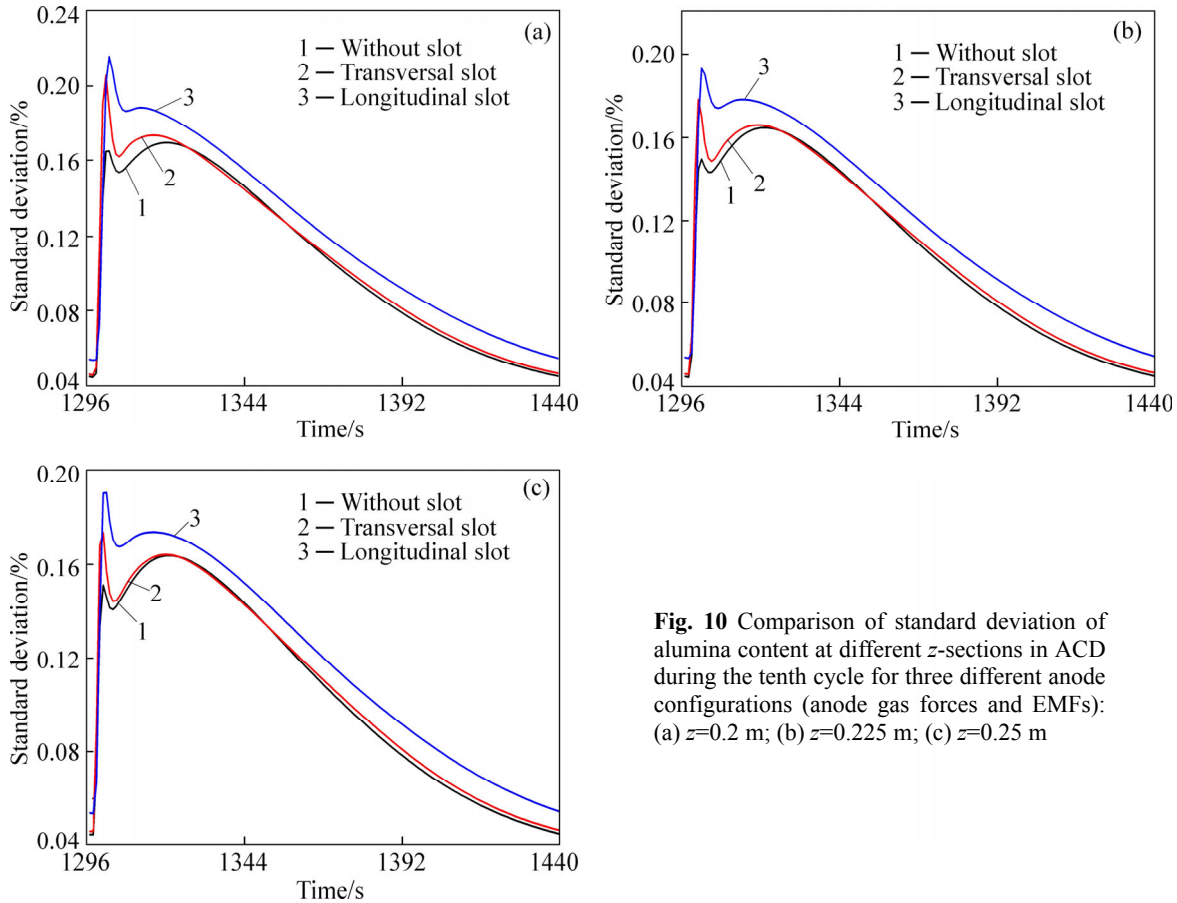

Fig. 10 Comparison of standard deviation of alumina content at different z-sections in ACD during the tenth cycle for three different anode configurations (anode gas forces and EMFs): (a) z=0.2 m; (b) z=0.225 m; (c) z=0.25 m

4 Conclusions

1) The simulation results show that adding a slot gives rise to an extremely strong escape of anode gas from the slots. Therefore, the longitudinal or transversal slot can reduce gas volume fraction and the height of gas layer under the anode bottom surface compared to the anode without a slot, and the former shows a more obvious effect, which may affect alumina content distribution.

2) The effect of the longitudinal or transversal slot is mainly to generate more small eddies around each anode and take effect on the two large eddies due to the EMFs. The bath average velocities for the anode without a slot, with a longitudinal slot and a transversal slot are 7.31, 6.13 and 6.76 cm/s, respectively.

3) The transient analysis of alumina content distributions shows that the characteristics of alumina content distribution follow the flow characteristics of the bath and the uniformity of alumina content distribution becomes better through time during one feeding cycle. A comparison of the standard deviations for three different anode configurations reveals that the slots can show a negative effect on the uniformity of alumina content because the effect of anode gas is weakened, and it is more obvious for longitudinal slot. It seems that the alumina content distribution is controlled to great extent by the anode gas force while the EMFs also play the second role.

References

[1] LIU Ye-xiang, LI Jie. Modern aluminum electrolysis [M]. Beijing: Metallurgical Industry Press, 2008: 69−77. (in Chinese)

[2] ZHOU Nai-jun, XUE Yu-qing, CHEN J J, TAYLOR M P. Numerical simulation of electrolyte two-phase flow induced by anode bubbles in an aluminum reduction cell [J]. Chemical Product and Process Modeling, 2007, 11(2): 1934−1945.

[3] ZHOU Nai-jun, XIA Xiao-xia, WANG Fu-qiang. Numerical simulation on electrolyte flow field in 156 kA drained aluminum reduction cells [J]. Journal of Central South University, 2007, 14(1): 42−46.

[4] ZHANG Hong-liang, WANG Zhi-gang, LI Jie, LAI Yan-qing. Simulation on flow field of anode gas and electrolyte in aluminum electrolysis with cermet inert anodes [J]. Journal of Central South University: Science and Technology, 2010, 41(4): 1256−1262. (in Chinese)

[5] ZHAN Shui-qing, ZHOU Jie-min, LI Mao, DONG Ying, ZHOU Yi-wen, YANG Jian-hong. Numerical simulation of gas–liquid two-phase flow in aluminum reduction cells with perforated anodes [J]. CIESC Journal, 2013, 64(10): 3612−3619. (in Chinese)

[6] ZHAN Shui-qing, LI Mao, ZHOU Jie-min, YANG Jian-hong, ZHOU Yi-wen. A CFD−PBM coupled model predicting anodic bubble size distribution in aluminum reduction cells [C]// GOHN G. Light Metals 2014. San Diego: TMS, 2014: 777−782.

[7] DOHEIM M A, ELKERSH A M, ALI M M. Computational modeling of flow in aluminum reduction cells due to gas bubbles and electromagnetic forces [J]. Metallurgical Materials Transactions B, 2007, 38(1): 113−119.

[8] ZHANG Kai-yu, FENG Yu-qing, SCHWARZ P, WANG Zhao-wen, COOKSEY M A. Computational fluid dynamics (CFD) modeling of bubble dynamics in the aluminum smelting process [J]. Industrial and Engineering Chemistry Research, 2013, 52(4): 11378−11390.

[9] FENG Y Q, COOKSEY M A, SCHWARZ M P. CFD modeling of alumina mixing in aluminium reduction cells [C]// HAGNI A M. Light Metals 2010. Seattle, WA: TMS, 2010: 451−456.

[10] FENG Y Q, COOKSEY M A, SCHWARZ M P. CFD modeling of alumina mixing in aluminium reduction cells [C]// LINDSAY J. Light Metals 2011. San Diego, CA: TMS, 2011: 543−548.

[11] THOMAS H. Numerical simulation and optimization of the alumina distribution in an aluminium electrolysis pot [D]. Lausanne: École Polytechnique Fédérale de Lausanne, 2011.

[12] ZHANG He-hui. Numerical study of vortex flow of melts and transport process of alumina in aluminum reduction cells [D]. Changsha: Central South University, 2012. (in Chinese)

[13] KAENEL R, ANTILLE J, ROMERIO M V, BESSON O. Impact of magnetohydrodynamic and bubbles driving forces on the alumina concentration in the bath of an Hall-Héroult cell [C]// BARRY S. Light Metals 2013. San Antonio: TMS, 2013: 585−590.

[14] ZHAN Shui-qing, LI Mao, ZHOU Jie-min, ZHOU Yi-wen, YANG Jian-hong. Numerical simulation of alumina concentration distribution in the melts of aluminum reduction cells [J]. The Chinese Journal of Nonferrous Metals, 2014, 24(10): 2658−2667. (in Chinese)

[15] ZHAN Shui-qing, LI Mao, ZHOU Jie-min, YANG Jian-hong, ZHOU Yi-wen. CFD simulation of dissolution process of alumina in an aluminum reduction cell with two-particle phase population balance model [J]. Applied Thermal Engineering, 2014, 73(1): 803−816.

[16] DIAS H P, MOURA R R. The use of transversal slot anodes at ALBRAS melter [C]// KVANDE H. Light Metals 2005. San Francisco, CA: TMS, 2005: 341−344.

[17] SEVERO D S, GUSBERTI V, PINTO E C V, MOURO R R. Modeling the bubble driven flow in the electrolyte as a tool for slotted anode design improvement [C]// SORLIE M. Light Metals 2007. Orlando, FL: TMS, 2007: 287−292.

[18] YANG W, COOKSEY M A. Effect of slot height and width on liquid flow in physical models of aluminum reduction cells [C]// SORLIE M. Light Metals 2007. Orlando, FL: TMS, 2007: 451−456.

[19] YANG Shuai, ZHANG Hong-liang, XU Yu-jie, ZHANG He-hui, ZOU Zhong, LI Jie, LAI Yan-qing. Effects of slot cutting at prebaked anodes on bubble elimination in aluminum reduction cell [J]. Journal of Central South University: Science and Technology, 2012, 43(12): 4617−4625. (in Chinese)

[20] SATO Y, SADATOMI M, SEKOGUCI K. Momentum and heat transfer in two–phase bubble flow–I: Theory [J]. Int J Multiphase Flow, 1975, 7(2): 167−177.

[21] FLUENT Inc. Fluent 6.3 User's Guide [EB/OL]. [2014-05-15]. http://aerojet.engr.ucdavis.edu/fluenthelp/html/ug/main_pre.htm.

[22] COOKSEY M A, YANG W. PIV measurements on physical models of aluminum reduction cells [C]// GALLOWAY T J. Light Metals 2006. Warrendale: TMS, 2006: 359−365.

(Edited by YANG Bing)